

Article

TimeMaxyne: A Shot-Noise Limited, Time-Resolved Pump-and-Probe Acquisition System Capable of 50 GHz Frequencies for Synchrotron-Based X-ray Microscopy

Markus Weigand ^{1,2,*}, Sebastian Wintz ¹ , Joachim Gräfe ¹, Matthias Noske ¹, Hermann Stoll ^{1,3} , Bartel Van Waeyenberge ⁴ and Gisela Schütz ¹

- ¹ Max-Planck-Institut für Intelligente Systeme, 70569 Stuttgart, Germany; wintz@is.mpg.de (S.W.); graefe@is.mpg.de (J.G.); matthias.noske@gmx.de (M.N.); stoll@is.mpg.de (H.S.); schuetz@is.mpg.de (G.S.)
² Helmholtz-Zentrum Berlin für Materialien und Energie, 14109 Berlin, Germany
³ Institut für Physik, Johannes Gutenberg-Universität Mainz, 55128 Mainz, Germany
⁴ Faculty of Sciences, Universiteit Gent, 9000 Gent, Belgium; bartel.vanwaeyenberge@ugent.be
* Correspondence: markus.weigand@helmholtz-berlin.de

Abstract: With the advent of modern synchrotron sources, X-ray microscopy was developed as a vigorous tool for imaging material structures with element-specific, structural, chemical and magnetic sensitivity at resolutions down to 25 nm and below. Moreover, the X-ray time structure emitted from the synchrotron source (short bunches of less than 100 ps width) provides a unique possibility to combine high spatial resolution with high temporal resolution for periodic processes by means of pump-and-probe measurements. To that end, TimeMaxyne was developed as a time-resolved acquisition setup for the scanning X-ray microscope MAXYMUS at the BESSY II synchrotron in order to perform high precision, high throughput pump-and-probe imaging. The setup combines a highly sensitive single photon detector, a real time photon sorting system and a dedicated synchronization scheme for aligning various types of sample excitations of up to 50 GHz bandwidth to the photon probe. Hence, TimeMaxyne has been demonstrated to be capable of shot-noise limited, time-resolved imaging, at time resolutions of 50 ps and below, only limited by the X-ray pulse widths of the synchrotron.

Keywords: time-resolve X-ray microscopy; pump-probe data acquisition; magnetic imaging



Citation: Weigand, M.; Wintz, S.; Gräfe, J.; Noske, M.; Stoll, H.; Van Waeyenberge, B.; Schütz, G. TimeMaxyne: A Shot-Noise Limited, Time-Resolved Pump-and-Probe Acquisition System Capable of 50 GHz Frequencies for Synchrotron-Based X-ray Microscopy. *Crystals* **2022**, *12*, 1029. <https://doi.org/10.3390/cryst12081029>

Academic Editor: Borislav Angelov

Received: 23 June 2022

Accepted: 17 July 2022

Published: 25 July 2022

Publisher's Note: MDPI stays neutral with regard to jurisdictional claims in published maps and institutional affiliations.



Copyright: © 2022 by the authors. Licensee MDPI, Basel, Switzerland. This article is an open access article distributed under the terms and conditions of the Creative Commons Attribution (CC BY) license (<https://creativecommons.org/licenses/by/4.0/>).

1. Introduction

Fundamental research on ordered spin systems such as topological skyrmion textures [1] or magnonic excitations [2] created a strong demand for magnetic probes with a high combined spatial and temporal resolution. The same holds true for the implementation and development of spintronic applications as in hard disk drives [3], GMR/TMR sensors and oscillators [4], as well as MRAM [5], or in view of future concepts such as racetrack data storage [6] or spin-wave computing [7]. While optical magnetic microscopy methods using visible light offer ultra-fast time resolutions [8], their spatial resolution is often insufficient for nanoscale systems. Alternately, electron and scanning probe microscopies [9,10] provide very high spatial magnetic resolution but typically suffer from limited time resolution. Addressing this gap in combined spatial and temporal magnetic resolutions, soft X-ray microscopies were established as powerful methods for quantitative, element specific and highly sensitive investigations of magnetic systems at length scales down to tens of nm and time scales down to tens of picoseconds. Currently, these methods are typically operated at synchrotron sources due to their requirements for highly brilliant and monochromatic X-ray radiation.

An important step for magnetic microscopy was the discovery of the X-ray magnetic circular dichroism effect (XMCD) in 1987 [11], which provided a contrast mechanism for magnetic X-ray microscopy. Based on this contrast mechanism, static magnetic X-ray microscopy was successively realized as X-ray photoemission electron microscopy

(XPEEM) (X-ray illumination, emitted photo-electron imaging) [12], full field transmission X-ray microscopy [TXM] (X-ray illumination, transmitted X-ray imaging) [13] and scanning transmission X-ray microscopy [STXM] (X-ray focus, transmitted X-ray detection) [14] (see Figure 1). All these techniques can utilize the pulsed nature of the synchrotron light as a stroboscopic probe for time resolved (TR) imaging. This was demonstrated in seminal magneto-dynamic studies in 2004 using TR-TXM [15] and TR-XPEEM [16] at the Advanced Light Source (ALS) in Berkeley. However, both TXM and XPEEM utilize two-dimensional detectors for imaging, whereas STXM only requires a point detector that, advantageously, can be read out at rates above the typical synchrotron frequency (F_s) of 500 MHz (repetition rate of the X-ray probes). Therefore, TR-STXM allows for the exploitation of the full photon flux of the synchrotron for multiphase acquisition without any need for dedicated timing operation modes of the storage ring. This was demonstrated by an impressive series of TR-STXM works on dynamic magnetic imaging, for example at the ALS [17–22], at the Stanford Synchrotron Radiation Lightsource (SSRL) [23,24], at the Canadian Light Source (CLS) in Saskatoon [21,25] and at the Swiss Light Source (SLS) in Villigen PSI [26–29]. We want to note that, besides these TR-STXM works, there are also more recent reports of TR-PEEM and TR-TXM, e.g., [30] and [31], respectively, as well as first examples of lensless TR X-ray holography [32], TR magnetic tomography using hard [33] and soft [34] X-rays, and TR X-ray ptychography [33,35].

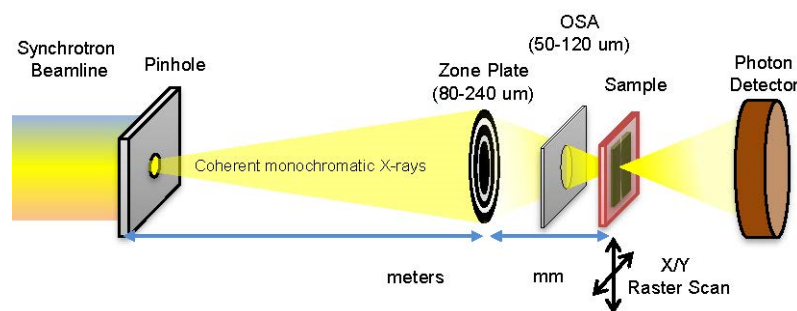


Figure 1. STXM operation principle (adapted from [36]): A FZP is illuminated by monochromatic, coherent X-ray light provided by a synchrotron beamline. The light is focused through an OSA (which blocks unwanted diffraction orders of the FZP) onto a focal spot on the sample. The transmitted photons are recorded by an X-ray photon detector, which allows probing of the local absorption of the sample, and therefore, usage of contrast mechanisms such as XAS (X-ray absorption spectroscopy), NEXAFS (Near edge X-ray absorption fine structure) and XMCD for elemental, chemical or magnetic contrast, respectively. The image is generated by raster scanning the sample through the stationary beam, with the lateral resolution being given by the size of the X-ray spot (which under fully coherent illumination is about 1.2 times the outermost zone width of the FZP).

Here, we describe the implementation of a shot-noise limited, multichannel acquisition system for pump-and-probe TR-STXM measurements, which was realized at the MAXYMUS endstation [36] situated at the BESSY II electron storage ring operated by the Helmholtz-Zentrum Berlin für Materialien und Energie. This system is referred to as TimeMaxyne: **T**ime-resolved **M**aximus data acquisition system (\ 'tīm mæ-'shēn\). The goal of the development of TimeMaxyne was to improve TR-STXM imaging respective to the existing solutions of the time, providing higher fidelity detection and a more flexible pump-and-probe scheme. The core of this system is a fast signal discriminator for the detection of single X-ray photons and a coupled FPGA board that is capable of sorting photon events into a maximum of 2048 time channels based on the photon arrival time relative to the excitation of the sample system. The dedicated synchronization methods discussed later ensure that these time channels are sampled interleaved and unbiased, eliminating most noise sources with frequencies below 1 MHz for shot-noise limited imaging, even on synchrotrons with complex operation modes.

As for the outline of the paper, following this introduction, there is a methods section covering general STXM imaging, the synchrotron as a stroboscopic X-ray source, single photon detection and the pump-and-probe excitation/detection scheme. Following that, a section presenting exemplary results acquired using TimeMaxyne will be presented. Finally, conclusions will be drawn together with a discussion of possible future developments for time-resolved X-ray microscopy.

2. Methods

2.1. STXM Imaging

STXM allows for the measurement of images with elemental, chemical or magnetic contrast by probing the local X-ray transmission of a sample, corresponding to an effective absorption cross-section over the sample thickness. For that purpose, monochromatic X-rays are focused by a Fresnel zone plate (FZP), i.e., a diffractive lens, to a spot of ~25 nm diameter on the sample (see Figure 1). Unwanted diffraction orders of the FZP are blocked by using an order-selecting aperture (OSA) in front of the sample. The sample itself is raster scanned in the focal plane of the FZP, and the transmission signal from a point detector behind the sample is recorded to yield a two-dimensional transmission image. For this technique, samples require sufficient X-ray transparency, which, in the soft X-ray range, limits their thickness (with few exceptions) to 10 s or 100 s of nm.

STXM provides spatially resolved access to a wide range of information about a sample system, exploiting the coherent X-rays with selectable polarization and photon energy from the synchrotron. Aside from resonant photon absorption energies, there is a strong contrast from the atomic number of the involved atoms and the local sample thickness. Moreover, by acquiring images below and above a known absorption edge, it is possible to gain quantitative maps of the corresponding element, while a hyperspectral image series across a particular absorption edge allows for the analysis of the chemical binding state of the investigated element for each pixel. Finally, when using circular polarized X-rays at resonant absorption edges, XMCD enables an element selective and quantitative determination of both spin and orbital magnetic moments, which can be used as magnetic contrast mechanism revealing the local magnetic orientation of the sample.

2.2. The Synchrotron as a Stroboscopic Light Source

In general, all time-resolved synchrotron methods exploit the stroboscopic X-ray illumination created by the time structure of the synchrotron storage ring: As the electrons are forced together into discrete bunches along the perimeter by the accelerating radio-frequency (RF) field, the emitted photon beams also have a pulsed time structure. In a typical soft X-ray synchrotron (e.g., BESSY II, ALS, SLS, CLS, etc., yet with the exception of SSRL), the RF frequency (F_S) is approximately 500 MHz, such that the X-ray photon flashes occur every 2 ns, thereby defining the repetition rate for a conventional pump-and-probe experiment. Many magnetic systems, however, will not have recovered from an excitation pump after this short time scale, creating the problematic situation where an integrating detector would average samples of different magnetic states. In order to avoid this signal corrupting effect, it is possible to reduce the repetition rate by discarding the vast majority of photon flux either by using only the so-called camshaft pulse or by using special operation modes of limited availability where gaps are left in the filling pattern between pulses to create a lower probe rate down to the MHz range. Neither of these methods is desirable, as they both come at the cost of a strongly reduced effect photon flux, and therefore, reduced signal-to-noise ratio.

TR-STXM measurements can overcome this restriction by making use of fast detectors: if one is able to tell apart the signals from two adjacent X-ray pulses, there is no longer a need for the sample to recover between successive pulses. Instead, one can sort the result from each pulse into an appropriate time channel with respect to a synchronized external stimulus (typically an electric pump). For the MAXYMUS endstation at BESSY II, this method provides a combined spatial and temporal resolution of ~25 nm and ~100 ps,

respectively [36]. The time resolution can be increased to ~50 ps when disregarding parts of the photon flux (filling pattern), and even to ~10 ps when exploiting the so-called low-alpha operation mode of BESSY II, which allows for much shorter X-ray pulses. However, note that as the pump-probe cycle needs to be repeatedly measured many times in order to gain a sufficient signal level (pixel integration ≥ 100 ms), TR-STXM is only sensitive to (at least on average) periodic/reproducible processes.

2.3. Single Photon Detection

A vital part of the pump-and-probe scheme is the capability to detect X-ray photons with sufficient time resolution to accurately attribute them to a certain electron bunch of the synchrotron, which at BESSY II are spaced 2 ns apart. In general, there is a lack of commercially available dedicated soft X-ray single photon detectors, however, as shown in [17,19,36], avalanche photodiodes (APDs) designed for the optical or infrared range are usable as X-ray detectors down to 500 eV when stripped of their original casings/glass windows.

For sufficient speed, a small APD (ideally 0.5 mm, or maximum 1 mm diameter of sensitive area) needs to be used, as larger APDs tend to be too slow due to their internal capacitance. Also, operation voltages must be adapted to the use of X-rays, as breakdown events need to be avoided in order to have the APD ready to detect photons every 2 ns, which requires lowering the APD reverse bias voltage for having a smaller gain compared to the specifications referring to infrared photon detection.

2.4. Pump-and-Probe Scheme

The general excitation scheme logic will be discussed below in terms of two different representations (which are in principle equivalent): Time domain and frequency domain.

2.4.1. Time-Domain

A straightforward stroboscopic illumination with a pump period (T_P) synchronized to the probe period ($T_S = 1/F_S = 2$ ns) will only result in the sample being probed every 2 ns. In order to achieve a denser temporal sampling, the pumping period is selected to induce a time shift τ with regard to the synchrotron clock after each pumping event. If this τ is an integer (M) fraction of the period between synchrotron flashes ($\tau = 2$ ns/ M), the original time relation will be restored after M pumping cycles, yielding a uniform temporal sampling of the excitation period with the time step τ between time channels (compare Figure 2). This is true for pumping periods that adhere to the rule of:

$$T_P = T_S \times (N/M), \quad (1)$$

where N is the total number of time channels in the acquisition, with M and N being coprime in order to avoid time step degeneration. Note that the time step τ here is equivalent to time-resolution as long as it is longer than the native pulse width of the X-ray flashes.

As the time delay between pump and probe is constantly shifting during the acquisition, we refer to this scheme as asynchronous excitation even though both pump and probe are still synchronized to the synchrotron clock, just not with the same ratio. One notable consequence of the asynchronous excitation is the fact that there is no fixed assignment between time channels and synchrotron bunches; every time the original time delay between pump and probe is regained after M excitation cycles, a different synchrotron bunch will provide the light for each time channel.

Deliberation shows that if the number of buckets (fillable bunches in one orbit) of the synchrotron N_B and the number of time channels to be acquired N do not share any prime factors, all synchrotron buckets will equally contribute to each time channel. For the case of BESSY II with 400 ($2^4 \times 5^2$) buckets, this means all values of N ending in 1, 3, 7 and 9 fulfill this condition. In case of such equal distribution, all filling pattern irregularities, both constant (gap, camshaft, special bunches) and fluctuating (distortions of the relative bunch intensities due to top-up operation or the non-uniform decay of bunch currents), do not affect the quality of the dynamic results. This is because for each pixel of a TR-STXM image,

all time channels are acquired quasi-simultaneously, i.e., interlaced on a nanosecond to microsecond scale, which means that distortions in a wide spectral range will affect all time channels equally and thus can be normalized out. Therefore, TR-STXM using asynchronous excitation allows for shot-noise limited dynamic imaging, as demonstrated in Figure 3.

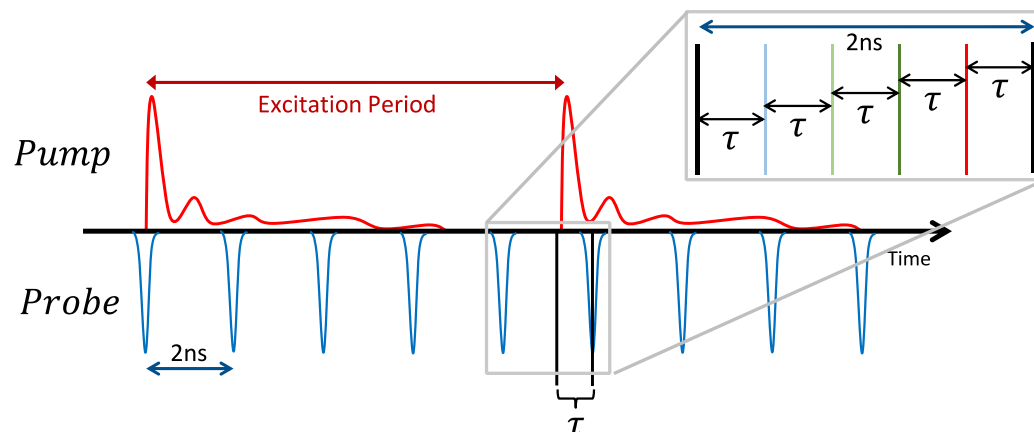


Figure 2. Illustration of the asynchronous pump-and-probe scheme used: The sample is probed every 2 ns by synchrotron flashes (probe period T_S). The pump period is a fractional multiple of the probe period, creating a shift of τ after each pump cycle between pump and probe. This delay adds up to the full 2 ns probe period after an integer number M of pump cycles (as shown in the inset), resulting in a time resolution of τ for the acquisition. In this example $N = 24$, $M = 5$, $T_P = 9.6$ ns, $\tau = 0.4$ ns.

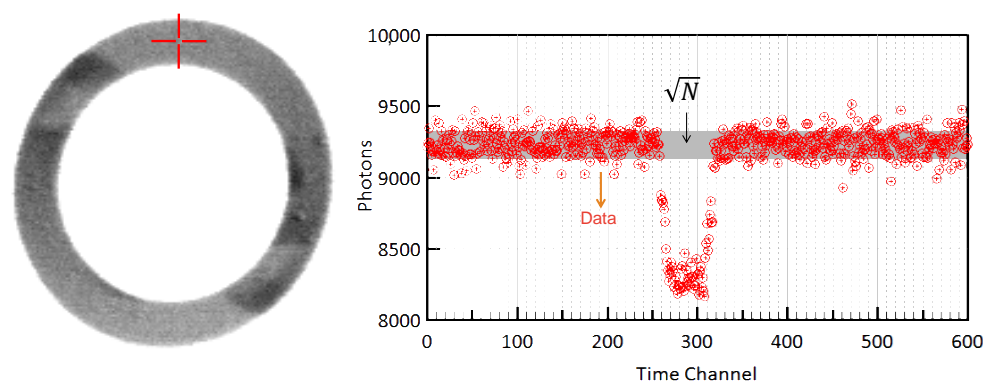


Figure 3. Example image of a pump-and-probe measurement showing the advantages of the synchronization scheme used, see also Ref. [37]. A snapshot of rotating domains in a $\text{Ni}_{81}\text{Fe}_{19}$ ring (top right) highlighting that, despite using the full filling pattern of the synchrotron with gap and camshaft pulses, the dynamic imaging is shot-noise limited in fidelity: In the right graph, the raw absorption data is plotted for a single point (indicated by the red cross), thereby not only directly showing the passing of a domain wall, but also having a noise figure that compares well with the gray bar, indicating a noise level of $(N)^{1/2}$.

2.4.2. Frequency Domain

Another way to excite the sample for the pump-and-probe detection is to use continuous periodic signals, such as an alternating sinusoidal radio frequency. In that case, the sample is not assumed to relax into the equilibrium state at the end of each pumping period, but rather exhibits a periodic dynamic steady-state, typically mainly of the same frequency as the excitation. Depending on the specific choice of N , and equivalently to Equation (1), the following frequency grid can be probed, and thus used for the excitation frequency (F_P):

$$F_P = F_S \times (M/N), \quad (2)$$

where the F_S in case of BESSY II is approximately 499.65 MHz. Figure 4 further illustrates the frequency domain excitation concept. Note that also here, M and N must be coprime in

order to avoid phase degeneration of time channels, and that the temporal width of the X-ray probe flashes sets a limit to the maximum probe frequency.

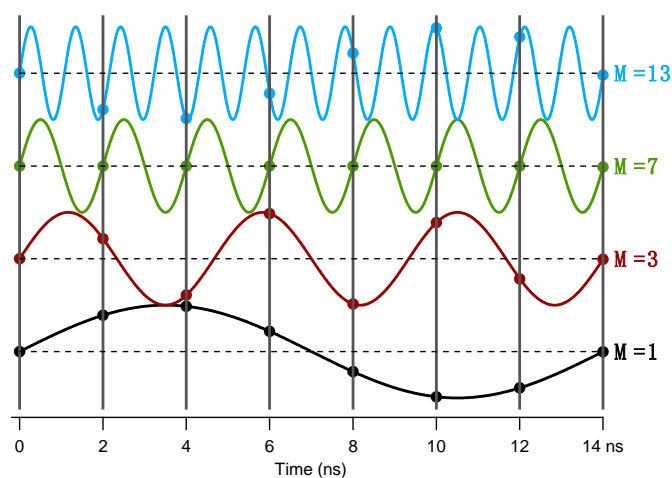


Figure 4. Illustration of the interleaved sampling of time channels using RF excitation of different frequencies in an example system with $N = 7$. Vertical lines represent the probe pulses, with markers representing the probed sample state. The black curve ($M = 1$) represents the lowest possible frequency to be probed with this number of channels, at $M \times 500/N$ MHz 71.42 MHz. In this case there is no interleaving, and the time channels are samples sequentially. This is not the case in the higher frequency red curve ($M = 3$), where 3 periods fit in the time needed to get 7 probe pulses, which means the samples need to be sorted in chronological order. The green curve ($M = 7$) represents a degenerate case (as $M = N$). All pulses sample the same phase of the excitation, leaving only a static stroboscopic image. This is equivalent to the limited dynamics possible using a time integrating detector. The blue curve ($M = 13$) is an example for a pumping frequency higher than the sample rate. Despite more than one period of excitation between sample points, the interleaved acquisition still yields the complete waveform (after the necessary sorting).

2.5. X-ray Probing

The TimeMaxyne pump-and-probe system was implemented using a combination of commercially available hardware and self-developed components, as schematically shown in Figure 5. Soft X-ray single photon detection is performed via a Hamamatsu S2381 Si-APD with a sensitive area of 500 μm diameter. This APD was originally designed for IR detection, nevertheless, it was found to be also suitable for soft X-rays when stripped of its optical glass cap. The APD output signal is amplified using a FEMTO HSA-X-2-60 amplifier, yielding single pulses of about 500 ps length (limited by amplifier bandwidth) and amplitudes of up to 500 mV amplitude, depending on the photon energy and APD bias voltage. The latter is set empirically by increasing the bias while observing count rates with and without X-ray illumination, and selecting the one resulting in the best combination of signal to noise ratio and quantum efficiency; a value that is typically around 10 V below the rated breakthrough voltage of the APD.

Detection and sorting of the photons is done on a customized FPGA-based counting board clocked at 499.65 MHz by directly synchronizing it to the RF clock of the storage ring. On this board, incoming photons are detected via the amplified pulses from the APD using a fast-gate discriminator, which compares the AC coupled input signal to a programmable reference value (500 μV resolution) and registers a photon arrival if the threshold is crossed within an approximately 25 ps wide time-window at the edge of every clock cycle. The threshold voltage has to be set high enough to not be triggered by amplifier noise and RF crosstalk between pump and detector wires, but low enough to have high detection efficiency (typically around 50 mV).

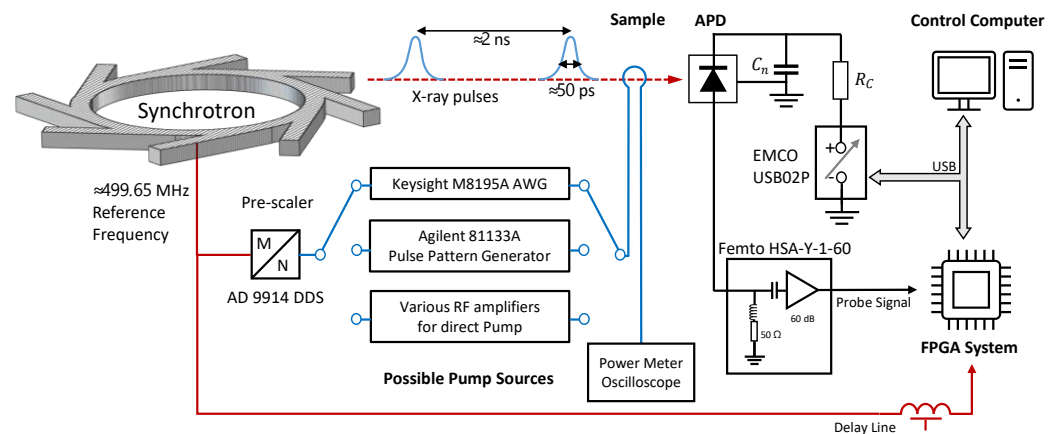


Figure 5. Simplified schematic overview of the TimeMaxyne setup. The storage ring frequency is used as a time base of both excitation and detection branch of the pump-and-probe setup. The APD bias voltage is applied using a precision high voltage power supply, while pulses from the APD induced by X-ray photons are amplified by 60 dB and recorded by the FPGA board, which communicates via USB with the control computer. Multiple excitation setups can be switched in, and the transmitted signal is analyzed on real time oscilloscopes or high bandwidth power meters.

To ensure optimal lock-in on the photon arrival time, the clock of the whole FPGA board and thereby the registration time-window can be shifted over a 2.5 ns range in 5 ps steps, using an integrated digital delay-line, which ensures that a correct alignment with the 2 ns spaced light pulses is always possible.

The total detection efficiency of the system is photon energy dependent and was measured to be about 50% at the Mn L edges (~650 eV) while increasing to about 80% at and above the Ni L₃ edge (~850 eV). Applying binary discrimination, the system will decide between registering a single event or not, for every probe cycle. This leads to a theoretical absolute maximum photon rate of 500 MPhotons/s, while for typical BESSY II filling patterns where about 100 buckets are unfilled, the maximum realistically achievable photon rate will be about 375 MPhotons/s. While the coherent flux typically does not reach these levels, being more in the 50–250 MPhotons/s range prior to the absorption in the sample, effects of non-linear detector response can affect measurements even at those rates as multi-photon events are only detected as single photons. This is particularly noticeable in samples with a large dynamic range of absorption, as non-linearities negatively affect the performance of the normalization algorithms.

The actual sorting of the photon counts happens in an ALTERA Cyclone III FPGA, which is running at 1/8th of the board frequency. The 500 Mbit/s stream from the discriminator indicating photon detection is deserialized by a factor of 8 and read into the FPGA with 1 byte/cycle. The first processing step in the FPGA is a logical AND operation with a ring buffer containing a gating bit for each bucket of the synchrotron, which allows preselection of certain bunches or gating out of parts of the filling pattern for special operation modes. At the same time the input stream also increments a photon counting register, of which a selectable bit can be linked to general purpose TTL outputs of the FPGA, where it creates a pulse signal with a rate proportional to a power of 2 fraction of the photon rate (as the full photon rate is too high to be compatible with common pulse counting hardware). This pulse signal can be used as real-time photon intensity signal for both calibration purposes and for feeding it into a counting card as data source for non-dynamic imaging.

The gated signals are fed into 8 histogram engines running in parallel, each operating on its own copy of a histogram buffer with a specific number of channels (N). Changing this number of accumulation channels is done by upload of specific FPGA code images. As each histogram engine only gets 1/8th of the input stream, the accumulation target is forwarded by 8 each cycle, i.e., histogram engine 0 writes to channel [0,8,16, ...], wrapping around at the end of the array, while histogram engine 1 writes to [1,9,17, ...], and so forth.

In the present revision, the maximum number of N is limited to 2048 given by the on-board memory restrictions of the used FPGA.

For each pixel, this accumulation continues as long as a trigger signal is high. When a pixel is finished, the engine completes the last excitation cycle, ensuring that each channel has the same number of possible photon events being accumulated. Afterwards, all 8 copies of the time channel array are being summed up, yielding one vector of N 22-bit numbers of counted photons as the time-dependent absorption signal from that particular pixel (corresponding to a maximum photon count of 2^{22} per channel and image pixel). The data is then sent via a USB interface to the LABVIEW control software where the individual pixels are composed to a series of 2D images, including options for video playback, filtering and normalization to better visualize small effects [38].

In its raw form, the collected time arrays are filled with photon counts in the order of photon arrival times. In most cases this order is not equivalent to chronological order relative to the excitation signal as a result of the asynchronous excitation and interlaced sampling. In order to resort the data to match chronological order, one needs to know the integer M selected for the pump frequency. Then, the sorted array S can be derived from the unsorted array U by the following operation, with i being an integer running from 1 to N (see also Figure 4):

$$S[i] = U[\text{modulo}(i \times M, N)]. \quad (3)$$

2.6. Electric Pumping

The synchronization of the pumping system to the rigid timing of the X-ray probes requires the pumping frequency to adhere to Equation (2) in order to ensure an asynchronous stroboscopic excitation of the device under test. To achieve this kind of synchronization is challenging, mainly for two reasons: First, the ring frequency is typically far enough from 500 MHz (BESSY II: 499.65 MHz) that a typically 10 MHz reference frequency input (via quartz tuning) of standard high frequency equipment will not accept it after a division by 50. Second, even when synchronized to the ring frequency, the pumping frequency will be an odd fraction of the ring clock which commercially available devices can typically not provide for the general case. Instead, the pump frequency (or frequency base when using an arbitrary wave form generator) is generated via a custom setup based on direct digital synthesis (DDS) which is extremely flexible in its capabilities.

2.6.1. Frequency and Pulse Generators

We used an Analog Devices AD9914 DDS, operating at 3.5 GHz with the synchrotron RF-clock multiplied by a factor of 7 as direct clock source. This allows phase stable M/N multiplication with M and N being arbitrary 32-bit integers, while also providing very fine control of both the output amplitude and phase (12-bit and 16-bit precision, respectively).

The output of the AD9914 DDS cover a frequency range of 50 kHz and 1.6 GHz, and the output signal can be used either as direct/amplified RF excitation of the device under test or as a trigger for an Agilent 81134A Pulse Pattern Generator. This generator can provide excitation pulses with rise and fall times down to 70 ps and a jitter of less than 8 ps. Furthermore, it has the ability to synchronize to arbitrary frequencies while producing pulse lengths that are independent of the synchronizing frequencies. By combining the pulse pattern generator output with the RF output using frequency mixers, excitation schemes of higher complexity can be achieved.

For frequencies above 1.6 GHz, an Analog Devices ADF5355 PLL was used. This device is a fractional- N synthesizer with programmable modulus (required for the asynchronous excitation criteria) and an integrated voltage-controlled oscillator. While this device is much more limited in terms of frequency ratios (i.e., only 8 bits for the divider, limiting the number of channels N to 256), it allows to apply output frequencies between 3.4 GHz and 6.8 GHz directly, down to 1.7 GHz with a divided ($1/2$) output and up to 13.6 GHz with a frequency doubled output. By using an additional external frequency doubler, frequencies of over 25 GHz have been achieved while still fulfilling the criteria for the asynchronous pump-and-

probe scheme. To ensure spectral purity this required the use of band-pass filters outside of the 3.4 to 6.8 GHz range. For low frequencies, this was done with different passive bandpass filters, while above 6.8 GHz an RF-Lambda MLBFP-42026 YIG filter was used.

2.6.2. Arbitrary Waveform Generators

While the original setup described above allowed for a wide range of frequencies and pulsed excitations, it suffered from having to use different pieces of equipment to cover the whole parameter space available for the pump-and-probe measurements. In addition, outside of the direct frequency ranges provided by the DDSs, signal fidelity both in power levels and spectral purity was non-optimal and non-consistent across the accessible frequency range.

The setup was thus recently upgraded by means of an arbitrary waveform generator (AWG) to serve as a universal pump source for both RF and pulsed pump signals, as well as to generate more complex signals such as multi-tone excitation or sinc pulses for broadband excitation [39]. The AWG in use is a Keysight M8195A, which has a sample rate of 65 GS/s and more than 25 GHz analog bandwidth. While the device provides internal pre-scalers for the synchronization input, their accuracy is not sufficient to allow phase locking with the storage ring (aside from limits in the resulting time resolution and possible channel numbers). To ensure a stable and synchronized operation of the AWG, an Arduino controlled AD9914 is used to dynamically pre-scale an AWG reference frequency, depending on the desired pump-and-probe parameters. This combination allows for an RF excitation of the device under test from about 250 kHz to above 30 GHz and it also allows to apply pulses and patterned excitations with excitation periods from 4 μ s down to the sub-ns range; all on up to four independent output channels [39]. The applicable RF frequencies can be extended up to 50 GHz when an external frequency doubler is used.

3. Exemplary Results

There have been many examples for the usage of TimeMaxyne at MAXYMUS/BESSY II for TR-STXM over the course of more than a decade. Among these examples is the direct observation of domain wall propagation in a magnetic ring [37], the data of which already was analyzed to an additional extent in Figure 3, revealing shot-noise limited data acquisition. A review, addressing partially results acquired by TimeMaxyne, is given by Ref. [22].

In particular, some exemplary works focused on the dynamics of spin textures, such as fast vortex core switching [40,41] and direct observation of skyrmion motion [42]. Other works address the spin texture driven excitation and direct observation of spin waves with wavelengths below the visible light detection limit [43–48]. Moreover, in the corresponding field of magnonics, spin-wave diffraction optics [49], a quantitative determination of the precession angle [50], efficient wavelength conversion [51], high-frequency spin-wave dynamics [52] and spin-wave self-scattering [53] were reported.

Figure 6 shows a TimeMaxyne TR-STXM spin-wave observation at 7.4 GHz frequency [45] using the BESSY II low-alpha operation mode. A magnetic vortex is formed in a ferromagnetic disk of ~ 3 μ m diameter, made of 80 nm thick permalloy ($\text{Ni}_{81}\text{Fe}_{19}$) (Figure 6a). Upon uniform alternating magnetic field excitation short-wavelength spin waves (wavelength ~ 140 nm) are emitted from the central vortex core as can be seen in snapshots of both absolute contrast (Figure 6b) (perpendicular magnetic and non-magnetic absorption) and normalized contrast (Figure 6c) (sensitive only to perpendicular magnetic changes); center regions are shown as a zoom-in at the respective bottom left corners. Figure 6d highlights the spin-wave propagation by means of line profiles at different delay times along the green arrow in Figure 6c. Thereby, these measurements demonstrate some of the unique capabilities of TR-STXM and TimeMaxyne in terms of combined spatial and temporal resolution.

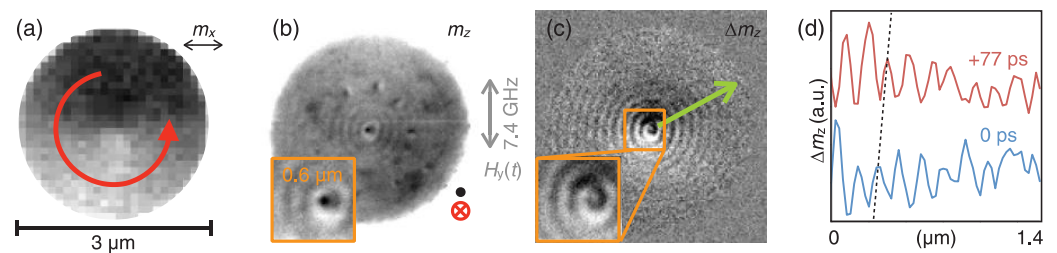


Figure 6. Example of spin-wave dynamics recorded using TimeMaxyne TR-STXM at MAXYMUS/BESSY II. (a) Magnetic vortex (red arrow) imaged with in-plane magnetic sensitivity (m_x). (b,c) Snapshots with perpendicular magnetic sensitivity of the response to a 7.4 GHz homogeneous alternating magnetic field excitation (grey arrow), zoom-ins of center regions in the bottom left corner. (b) Absolute contrast containing magnetic and non-magnetic absorption, (c) normalized contrast revealing only the magnetic changes. (d) Line profiles at different delay times along the green arrow in (c). Reprinted with permission from [45]. Copyright 2019 American Physical Society.

Many of the above examples make use of an in-situ magnet system providing magnetic fields up to 250 mT collinear or normal (horizontal) to the X-ray beam [54]. Future works may involve the application of a liquid helium cryostat with a minimum temperature of 25 K [55] and a picosecond laser system [56] for TR-STXM available at MAXYMUS.

4. Discussion and Outlook

The TimeMaxyne pump-and-probe technique has proven over the years to be a highly powerful and reliable tool for TR-STXM at MAXYMUS/BESSY II. The ability to utilize photon rates of more than 10^8 /s while having shot-noise limited performance allows for interactive investigations with short acquisition times, as well as for systematic exploration of samples with excitation parameter scans in reasonable timeframes while maintaining high data quality. The versatility of the number of time channels in combination with the asynchronous excitation scheme means that imaging is possible over several orders of magnitude of frequencies and time resolution, providing optimum opportunities to investigate a sample system in a wide range of excitation environments. Nevertheless, there are a few drawbacks and challenges that are beyond the scope of the current hard- and software solution that remain to be solved.

At first, the concept of TimeMaxyne is based on the idea of single photon detection and processing of a Boolean data for photon arrival, which is just still enough for the coherent flux available at undulator beamlines of 3rd generation synchrotrons. However, there is no headroom for single-photon-counting-based solutions to benefit from higher flux beamlines, for example at 4th generation synchrotrons. This is a vital flaw considering that time-resolved imaging is starved for photon flux in most usage cases, and as such, is a prime candidate to benefit from high brilliance sources. While it would be possible to rebuild the system using a high-speed analog-to-digital converter instead of a binary discriminator together with a more powerful FPGA setup being able to deal with the increased data rates, the level in complexity involved in such a high-speed system makes it difficult to develop the customized soft- and hardware.

The second problem is the reliance of the method on the idea that photon arrival time perfectly correlates to the ring frequency. Therefore, any random or systematic deviations of photon pulse times from the ring clock will directly increase the effective pulse length and thus reduce the time resolution, as all bunches contribute to each time channel. The use of higher harmonic cavities for beam conditioning at synchrotron sources can introduce such deviations of the local timing of bunches. A slight detuning of the real bunch frequency causes the bunches to build up an increasing phase shift along the filled bunches of the ring, which recovers over the unfilled gap. In case of BESSY II, this effect increases the effective pulse width in standard operation mode from about 45 ps to about 110 ps, which is more than a factor of two. This deteriorating effect can be partially countered by discarding large parts of the filling pattern (which is possible with the integrated gating function of

the FPGA) at the cost of the majority of photon flux. An improved solution would employ real-time correction of the photon histogramming, depending on the actual photon phase shift, which is beyond the capabilities of the system presented here.

As a third point, future acquisition systems should also allow an increase of the maximum possible number of channels N to significantly beyond 2048 in order to extend the maximum observation period while simultaneously allowing for a decrease of the time step.

An interesting concept for a slightly different way to perform TR-STXM experiments is given by time taggers that record the arrival time of individual photons. While such devices are currently still somewhat limited in their maximum count rate (~ 100 MPhotons/s), they could, in principle, allow for probing events/dynamics independent of the probe frequency (free operation mode), although such signals would be rather sparse in the data flow. In combination with a constant fraction discriminator on the other hand, time taggers allow for the improvement of the time resolution of TR-STXM [57] compared to that given by the synchrotron pulse distribution, as ideally the individual arrival time of each photon is recorded. Thereby, the time resolution potentially could be improved to the level of the timing precision of the time tagger (~ 10 ps).

It should be noted that the present TimeMaxyne system is not inherently limited to TR-STXM, and could be transferred to any other time-resolved soft X-ray measurement technique that utilizes a point detector. Likewise, the improved X-ray probe length distribution from a future upgrade of the BESSY II synchrotron to a variable pulse length storage ring (VSR) can be fully exploited for a higher time-resolution using TimeMaxyne. Finally, TimeMaxyne is not limited to XMCD as contrast mechanism; it can be used for time-resolved X-ray magnetic linear dichroism studies in the light of antiferromagnetic spintronics or for 3D magnetic imaging. Furthermore TR-STXM could be extended to other ordering parameters of condensed matter (polarization or mechanics) as well as to time-resolved chemistry.

Author Contributions: M.W., H.S., B.V.W. and G.S. conceived the project. B.V.W. programmed the FPGA. M.W. and B.V.W., with the support of all authors, implemented the TimeMaxyne data acquisition at Maxymus. M.N. implemented the Labview acquisition and control software. S.W. and H.S. conceived TR-STXM operation in the low-alpha mode. M.W. and J.G. conceived the programming of the AWG excitation source. M.W. and S.W., with the support of all authors, wrote the manuscript. All authors have read and agreed to the published version of the manuscript.

Funding: This research received no external funding.

Acknowledgments: We thank Michael Bechtel for technical support. We are grateful to all authors of the scientific papers employing TimeMaxyne at Maxymus, thereby contributing to its further development. We are appreciative to various present and former members of the Schütz department at MPI-IS (formerly MPI-MF) for the general support of Maxymus. We thank Helmholtz-Zentrum Berlin for the allocation of synchrotron radiation beamtime.

Conflicts of Interest: The authors declare no conflict of interest.

References

1. Rößler, U.K.; Bogdanov, A.N.; Pfleiderer, C. Spontaneous skyrmion ground states in magnetic metals. *Nature* **2006**, *442*, 797–801. [[CrossRef](#)] [[PubMed](#)]
2. Bloch, F. Zur Theorie des Ferromagnetismus. *Z. Phys.* **1930**, *61*, 206–219. [[CrossRef](#)]
3. Shiroishi, Y.; Fukuda, K.; Tagawa, I.; Iwasaki, H.; Takenoiri, S.; Tanaka, H.; Mutoh, H.; Yshikawa, N. Future Options for HDD Storage. *IEEE Trans. Magn.* **2009**, *45*, 3816–3822. [[CrossRef](#)]
4. Katine, J.A.; Fullerton, E.E. Device implications of spin-transfer torques. *J. Magn. Magn. Mater.* **2008**, *320*, 1217–1226. [[CrossRef](#)]
5. Tehrani, S.; Slaughter, J.M.; Chen, E.; Durlam, M.; Shi, J.; DeHerrera, M. Progress and outlook for MRAM technology. *IEEE Trans. Magn.* **1999**, *35*, 2814–2819. [[CrossRef](#)]
6. Parkin, S.S.P.; Hayashi, M.; Thomas, L. Magnetic domain-wall racetrack memory. *Science* **2008**, *320*, 190–194. [[CrossRef](#)]
7. Chumak, A.V.; Kabos, P.; Wu, M.; Abert, C.; Adelman, C.; Adeyeye, A.O.; Akerman, J.; Aliev, F.G.; Anane, A.; Awad, A.; et al. Roadmap on Spin-Wave Computing. *IEEE Trans. Magn.* **2022**, *58*, 0800172. [[CrossRef](#)]
8. Lee, K.D.; Kim, J.-W.; Jeong, J.-W.; Kim, D.-H.; Shin, S.-C.; Hong, K.-H.; Lee, Y.S.; Nam, C.H.; Son, M.H.; Hwang, S.W. Femtosecond pump-probe MOKE microscopy for an ultrafast spin dynamics study. *J. Korean Phys. Soc.* **2006**, *49*, 2402–2407.

9. Raabe, J.; Pulwey, R.; Sattler, R.; Schweinböck, T.; Zweck, J.; Weiss, D. Magnetization pattern of ferromagnetic nanodisks. *J. Appl. Phys.* **2000**, *88*, 4437–4439. [[CrossRef](#)]
10. Wachowiak, A.; Wiebe, J.; Bode, M.; Pietzsch, O.; Morgenstern, M.; Wiesendanger, R. Direct observation of internal spin structure of magnetic vortex cores. *Science* **2002**, *298*, 577–580. [[CrossRef](#)]
11. Schütz, G.; Wagner, W.; Wilhelm, W.; Kienle, P.; Zeller, R.; Frahm, R.; Materlik, G. Absorption of Circularly Polarized X-Rays in Iron. *Phys. Rev. Lett.* **1987**, *58*, 737–740. [[CrossRef](#)] [[PubMed](#)]
12. Stöhr, J.; Wu, Y.; Hermsmeider, B.D.; Samant, M.G.; Harp, G.R.; Koranda, S.; Dunham, D.; Tonner, B.P. Element-Specific Magnetic Microscopy with Circularly Polarized X-rays. *Science* **1993**, *259*, 658–661. [[CrossRef](#)]
13. Fischer, P.; Schütz, G.; Schmahl, G.; Guttman, P.; Raasch, D. Imaging of magnetic domains with the X-ray microscope at BESSY using X-ray magnetic circular dichroism. *Z. Phys. B-Condens. Matter* **1996**, *101*, 313–316. [[CrossRef](#)]
14. Kortright, J.B.; Kim, S.-K.; Ohldag, H.; Meigs, G.; Warwick, A. Magnetization imaging using scanning transmission x-ray microscopy. *X-ray Microsc. Proc.* **2000**, *507*, 49–54.
15. Stoll, H.; Puzic, A.; Van Waeyenberge, B.; Fischer, P.; Raabe, J.; Buess, M.; Haug, T.; Höllinger, R.; Back, C.; Weiss, D.; et al. High-resolution imaging of fast magnetization dynamics in magnetic nanostructures. *Appl. Phys. Lett.* **2004**, *84*, 3328–3330. [[CrossRef](#)]
16. Choe, S.B.; Acremann, A.; Schöll, A.; Bauer, A.; Doran, A.; Stöhr, J.; Padmore, H.A. Vortex core-driven magnetization dynamics. *Science* **2004**, *304*, 420–422. [[CrossRef](#)] [[PubMed](#)]
17. Van Waeyenberge, B.; Puzic, A.; Stoll, H.; Chou, K.W.; Tylliszczak, T.; Hertel, R.; Fähnle, M.; Brückl, H.; Rott, K.; Reiss, G.; et al. Magnetic vortex core reversal by excitation with short bursts of an alternating field. *Nature* **2006**, *444*, 461–464. [[CrossRef](#)]
18. Acremann, Y.; Strachan, J.P.; Chembrolu, V.; Andrews, S.D.; Tylliszczak, T.; Katine, J.A.; Carey, M.J.; Clemens, B.M.; Siegmund, H.C.; Stöhr, J. Time-resolved imaging of spin transfer switching: Beyond the macrospin concept. *Phys. Rev. Lett.* **2006**, *96*, 217202. [[CrossRef](#)]
19. Acremann, Y.; Chembrolu, V.; Strachan, J.P.; Tylliszczak, T.; Stöhr, J. Software defined photon counting system for time resolved X-ray experiments. *Rev. Sci. Instrum.* **2007**, *78*, 014702. [[CrossRef](#)]
20. Yu, X.W.; Pribiag, V.S.; Acremann, Y.; Tulapurkar, A.A.; Tylliszczak, T.; Chou, K.W.; Bräuer, B.; Li, Z.-P.; Lee, O.J.; Gowtham, P.G.; et al. Images of a Spin-Torque-Driven Magnetic Nano-Oscillator. *Phys. Rev. Lett.* **2011**, *106*, 167202. [[CrossRef](#)]
21. Weigand, M.; Van Waeyenberge, B.; Vansteenkiste, A.; Curcic, M.; Sackmann, V.; Stoll, H.; Tylliszczak, T.; Kaznatcheev, K.; Bertwistle, D.; Woltersdorf, G.; et al. Vortex Core Switching by Coherent Excitation with Single In-Plane Magnetic Field Pulses. *Phys. Rev. Lett.* **2009**, *102*, 077201. [[CrossRef](#)] [[PubMed](#)]
22. Stoll, H.; Noske, M.; Weigand, M.; Richter, K.; Krüger, B.; Reeve, R.M.; Hänze, M.; Adolff, C.F.; Stein, F.-U.; Meier, G.; et al. Imaging spin dynamics on the nanoscale using X-ray microscopy. *Front. Phys.* **2015**, *3*, 26. [[CrossRef](#)]
23. Bonetti, S.; Kukreja, R.; Chen, Z.; Spodig, D.; Ollefs, K.; Schöppner, C.; Meckenstock, R.; Ney, A.; Pinto, J.; Houanche, R.; et al. Microwave soft X-ray microscopy for nanoscale magnetization dynamics in the 5–10 GHz frequency range. *Rev. Sci. Instrum.* **2015**, *86*, 093703. [[CrossRef](#)]
24. Bonetti, S.; Kukreja, R.; Chen, Z.; Macia, F.; Hernandez, J.M.; Eklund, A.; Bakckes, D.; Frisch, J.; Katine, J.; Malm, G.; et al. Direct observation and imaging of a spin-wave soliton with p-like symmetry. *Nat. Commun.* **2015**, *6*, 8889. [[CrossRef](#)] [[PubMed](#)]
25. Cheng, C.; Bailey, W.E. Sub-micron mapping of GHz magnetic susceptibility using scanning transmission X-ray microscopy. *Appl. Phys. Lett.* **2012**, *101*, 182407. [[CrossRef](#)]
26. Puzic, A.; Korhonen, T.; Kalantari, B.; Raabe, J.; Quitmann, C.; Jüllig, P.; Bommer, L.; Goll, D.; Schütz, G.; Wintz, S.; et al. Photon Counting System for Time-resolved Experiments in Multibunch Mode. *Synchrotron Radiat. News* **2010**, *23*, 26–32. [[CrossRef](#)]
27. Wohlhüter, P.; Bryan, M.T.; Warnicke, P.; Gliga, S.; Stevenson, S.E.; Heldt, G.; Saharan, L.; Suszka, A.K.; Moutafis, C.; Chopdekar, R.V.; et al. Nanoscale switch for vortex polarization mediated by Bloch core formation in magnetic hybrid systems. *Nat. Commun.* **2015**, *6*, 7836. [[CrossRef](#)]
28. Baumgartner, M.; Garello, K.; Mendil, J.; Avci, C.O.; Grimaldi, E.; Murer, C.; Feng, J.; Gabureac, M.; Stamm, C.; Acremann, Y.; et al. Spatially and time-resolved magnetization dynamics driven by spin-orbit torques. *Nat. Nanotechnol.* **2017**, *12*, 980–986. [[CrossRef](#)]
29. Finizio, S.; Watts, B.; Raabe, J. Why is my image noisy? A look into the terms contributing to a time-resolved X-ray microscopy image. *J. Synchrotron Radiat.* **2021**, *28*, 1146–1158. [[CrossRef](#)]
30. Foerster, M.; Macia, F.; Statuto, N.; Finizio, S.; Hernandez-Minguez, A.; Lendinez, S.; Santos, P.V.; Fontcuberta, J.; Hernandez, J.M.; Kläui, M.; et al. Direct imaging of delayed magneto-dynamic modes induced by surface acoustic waves. *Nat. Commun.* **2017**, *8*, 407. [[CrossRef](#)]
31. Im, M.Y.; Han, H.-S.; Jung, M.S.; Yu, Y.-S.; Lee, S.; Yoon, S.; Chao, W.; Fischer, P.; Hong, J.-I.; Lee, K.-S. Dynamics of the Bloch point in an asymmetric permalloy disk. *Nat. Commun.* **2019**, *10*, 539. [[CrossRef](#)] [[PubMed](#)]
32. Büttner, F.; Moutafis, C.; Schneider, M.; Krüger, B.; Günther, C.M.; Geilhufe, J.; Korff Schmising, C.v.; Mohanty, J.; Pfau, B.; Schaffert, S.; et al. Dynamics and inertia of skyrmionic spin structures. *Nat. Phys.* **2015**, *11*, 225–228. [[CrossRef](#)]
33. Donnelly, C.; Finizio, S.; Gliga, S.; Holler, M.; Hrabec, A.; Odstrcil, M.; Mayr, S.; Scagnoli, V.; Heyderman, L.J.; Guizar-Sicairos, M.; et al. Time-resolved imaging of three-dimensional nanoscale magnetization dynamics. *Nat. Nanotechnol.* **2020**, *15*, 356–360. [[CrossRef](#)] [[PubMed](#)]

34. Finizio, S.; Donnelly, C.; Mayr, S.; Hrabec, A.; Raabe, J. Three-dimensional Vortex Gyration Dynamics Unraveled by Time-Resolved Soft X-ray Laminography with freely selectable excitation frequencies. *Nano Lett.* **2022**, *22*, 1971–1977. [[CrossRef](#)] [[PubMed](#)]
35. Langer, M. (unpublished).
36. Weigand, M. *Realization of a New Magnetic Scanning X-ray Microscope and Investigation of Landau Structures under Pulsed Field Excitation*; Cuvillier: Göttingen, Germany, 2015.
37. Bisig, A.; Mawass, M.A.; Stärk, M.; Moutafis, C.; Rhensius, J.; Heidler, J.; Gliga, S.; Weigand, M.; Tyliszczak, T.; Van Waeyenberge, B.; et al. Dynamic domain wall chirality rectification by rotating magnetic fields. *Appl. Phys. Lett.* **2015**, *106*, 122401. [[CrossRef](#)]
38. Noske, M. *Ultraschnelles Vortexkernschalten*; Cuvillier: Göttingen, Germany, 2015.
39. Groß, F.; Träger, N.; Schulz, F.; Weigand, M.; Dippon, T.; Gräfe, J. A high frequency builder software for arbitrary radio frequency signals. *Rev. Sci. Instrum.* **2022**, *93*, 034704. [[CrossRef](#)]
40. Kammerer, M.; Weigand, M.; Curcic, M.; Noske, M.; Sproll, M.; Vansteenkiste, A.; Van Waeyenberge, B.; Stoll, H.; Woltersdorf, G.; Back, C.H.; et al. Magnetic vortex core reversal by excitation of spin waves. *Nat. Commun.* **2011**, *2*, 279. [[CrossRef](#)]
41. Noske, M.; Gangwar, A.; Stoll, H.; Kammerer, M.; Sproll, M.; Dieterle, G.; Weigand, M.; Fähnle, M.; Woltersdorf, G.; Back, C.H.; et al. Unidirectional sub-100-ps magnetic vortex core reversal. *Phys. Rev. B* **2014**, *90*, 104415. [[CrossRef](#)]
42. Litzius, K.; Lemesh, I.; Krüger, B.; Bassirian, P.; Caretta, L.; Richter, K.; Büttner, F.; Sato, K.; Tretiakov, O.A.; Förster, J.; et al. Skyrmion Hall effect revealed by direct time-resolved X-ray microscopy. *Nat. Phys.* **2017**, *13*, 170–175. [[CrossRef](#)]
43. Wintz, S.; Tiberkevich, V.; Weigand, M.; Raabe, J.; Lindner, J.; Erbe, A.; Slavin, A.; Fassbender, J. Magnetic vortex cores as tunable spin-wave emitters. *Nat. Nanotechnol.* **2016**, *11*, 948–953. [[CrossRef](#)]
44. Sluka, V.; Schneider, T.; Gallardo, R.A.; Kakay, A.; Weigand, M.; Warnatz, T.; Mattheis, R.; Roldan-Molina, A.; Landeros, P.; Tiberkevich, V.; et al. Emission and propagation of 1D and 2D spin waves with nanoscale wavelengths in anisotropic spin textures. *Nat. Nanotechnol.* **2019**, *14*, 328–333. [[CrossRef](#)] [[PubMed](#)]
45. Dieterle, G.; Förster, J.; Stoll, H.; Semisalova, A.S.; Finizio, S.; Gangwar, A.; Weigand, M.; Noske, M.; Fähnle, M.; Bykova, I.; et al. Coherent Excitation of Heterosymmetric Spin Waves with Ultrashort Wavelengths. *Phys. Rev. Lett.* **2019**, *122*, 117202. [[CrossRef](#)] [[PubMed](#)]
46. Behncke, C.; Adolff, C.F.; Lenzing, N.; Hänze, M.; Schulte, B.; Weigand, M.; Schütz, G.; Meier, G. Spin-wave interference in magnetic vortex stacks. *Commun. Phys.* **2018**, *1*, 50. [[CrossRef](#)]
47. Förster, J.; Gräfe, J.; Bailey, J.; Finizio, S.; Träger, N.; Groß, F.; Mayr, S.; Stoll, H.; Dubs, C.; Surzhenko, O.; et al. Direct observation of coherent magnons with suboptical wavelengths in a single-crystalline ferrimagnetic insulator. *Phys. Rev. B* **2019**, *100*, 214416. [[CrossRef](#)]
48. Mayr, S.; Flajsman, L.; Finizio, S.; Hrabec, A.; Weigand, M.; Förster, J.; Stoll, H.; Heyderman, L.J.; Urbanek, M.; Wintz, S.; et al. Spin-Wave Emission from Vortex Cores under Static Magnetic Bias Fields. *Nano Lett.* **2021**, *21*, 1584–1590. [[CrossRef](#)] [[PubMed](#)]
49. Gräfe, J.; Gruszecki, P.; Zelent, M.; Decker, M.; Keskinbora, K.; Noske, M.; Gawronski, P.; Stoll, H.; Weigand, M.; Krawczyk, M.; et al. Direct observation of spin-wave focusing by a Fresnel lens. *Phys. Rev. B* **2020**, *102*, 024420. [[CrossRef](#)]
50. Groß, F.; Träger, N.; Förster, J.; Weigand, M.; Schütz, G.; Gräfe, J. Nanoscale detection of spin wave deflection angles in permalloy. *Appl. Phys. Lett.* **2019**, *114*, 012406. [[CrossRef](#)]
51. Groß, F.; Zelent, M.; Träger, N.; Förster, J.; Sanli, U.T.; Sauter, R.; Decker, M.; Back, C.H.; Weigand, M.; Keskinbora, K.; et al. Building Blocks for Magnon Optics: Emission and Conversion of Short Spin Waves. *ACS Nano* **2020**, *14*, 17184–17193. [[CrossRef](#)]
52. Träger, N.; Gruszecki, P.; Lisiecki, F.; Förster, J.; Weigand, M.; Wintz, S.; Stoll, H.; Glowinski, H.; Kuswik, P.; Krawczyk, M.; et al. Direct Imaging of High-Frequency Multimode Spin Wave Propagation in Cobalt-Iron Waveguides Using X-ray Microscopy beyond 10 GHz. *Phys. Status Solidi-Rapid Res. Lett.* **2020**, *14*, 2000373. [[CrossRef](#)]
53. Träger, N.; Gruszecki, P.; Lisiecki, F.; Groß, F.; Förster, J.; Weigand, M.; Glowinski, H.; Kuswik, P.; Dubowik, J.; Schütz, G.; et al. Real-Space Observation of Magnon Interaction with Driven Space-Time Crystals. *Phys. Rev. Lett.* **2021**, *126*, 057201. [[CrossRef](#)]
54. Nolle, D.; Weigand, M.; Audehm, P.; Georing, E.; Wiesemann, U.; Wolter, C.; Nolle, E.; Schütz, G. Note: Unique characterization possibilities in the ultra high vacuum scanning transmission X-ray microscope (UHV-STXM) “MAXYMUS” using a rotatable permanent magnetic field up to 0.22 T. *Rev. Sci. Instrum.* **2012**, *83*, 046112. [[CrossRef](#)] [[PubMed](#)]
55. Simmendinger, J.; Ruoss, S.; Stahl, C.; Weigand, M.; Gräfe, J.; Schütz, G.; Albrecht, J. Transmission X-ray microscopy at low temperatures: Irregular supercurrent flow at small length scales. *Phys. Rev. B* **2018**, *97*, 134515. [[CrossRef](#)]
56. Kern, L.-M.; Pfau, B.; Deinhart, V.; Schneider, M.; Klose, C.; Gerlinger, K.; Wittrock, S.; Engel, D.; Will, I.; Günther, C.M.; et al. Deterministic Generation and Guided Motion of Magnetic Skyrmions by Focused He⁺-Ion Irradiation. *Nano Lett.* **2022**, *22*, 4028. [[CrossRef](#)] [[PubMed](#)]
57. Finizio, S.; Mayr, S.; Raabe, J. Time-of-arrival detection for time-resolved scanning transmission X-ray microscopy imaging. *J. Synchrotron Radiat.* **2020**, *27*, 1320–1325. [[CrossRef](#)]